CHAPTER 3: Zn doped Ag_2O photocatalysts

3.1 Introduction

Single component photocatalysts suffer from several disadvantages. For instance, only wideband semiconductors have conduction (CB) and valence band (VB) positions that offer sufficient driving force for photo-oxidation or reduction reactions. However, such photocatalysts suffer from recombination and photo-efficiency issues. They require UV radiation for photo-excitation, which is only 4% of the solar spectrum (Jing Liu et al., 2017). Indeed nowadays, preference is for visible light photocatalysts over those that need UV range radiation.

Doping of wideband semiconductors by metal or non-metal ions is one technique that has been widely used in literature to tackle these issues. It introduces defects in the crystal lattice of the pure phase semiconductor that may increase the catalytic activation of particular bonds in substrate molecules. Alternatively, defects can trap the holes or electrons and prevent their recombination. Another significant effect is the introduction of new dopant bands that may narrow or widen the bandgap of the photocatalyst. Such doping can introduce intermediate energy levels that contract the original bandgap, making the initially wideband semiconductor photo-responsive to visible light irradiation. Following this, quite a few researchers have reported doping of ZnO, TiO_2, and other wideband semiconductors by suitable metals that gave rise to intermediate dopant bands (Janisch et al., 2005). For instance, reports show that the bandgap of ZnO can be reduced to a value in the visible range by adding a small amount of Ag or Au (Lin et al., 2009).

The opposite approach is a less commonly followed strategy. In this case, a semiconductor is doped with a metal ion to increase the bandgap of the native semiconductor. An example of such bandgap widening is the Zn doping of CdS (Ma et al., 2017; F. Yang et al., 2012). In these investigations, the authors showed that Zn doping CdS modified the VB and CB positions of the resulting semiconductor (F. Yang et al., 2012). The change in the VB position was more than that in the CB energy. Likewise, Ohtomo et al. (Ohtomo et al. 1998) demonstrated that Mg doping of ZnO significantly widens the bandgap to the solar-blind region. In another publication, Choopun et al. (Choopun et al., 2002) reported ultra-wide bandgaps above 5.0 eV in cubic phase $Mg_xZn_{1-x}O$ thin films. Recently, Xie et al. (Xie et al., 2019) investigated the effect of lattice restraint on the widening of the ZnO bandgap due to the doping of Mg^{2+} cations along with Be ions as a co-dopant.

The present study follows this strategy and attempts to dope Zn^{2+} in the Ag_2O lattice to widen its bandgap. While silver oxide is a p-type semiconductor with a small bandgap, ranging from 1.2 to 1.5 eV, ZnO is a semiconductor having a wide bandgap. It is essential to mention that there are no investigations reported in the literature on this particular problem. The main feature of Zn^{2+} ion doping in Ag_2O is that the former ion is more than 50% smaller than Ag^+ cations. Given this size mismatch, doping only low percentages of Zn^{2+} ions in the Ag_2O lattice is possible. Also, investigating the position of Zn in the Ag_2O lattice is a noteworthy issue. Introducing a dilute concentration of Zn salt under high temperature and pressure conditions could lead to its inclusion in the Ag_2O lattice.

Methods like vapor deposition, sol-gel, calcination, solvothermal, etc., have been successfully used to fabricate doped metal oxides nanostructure (Campos-Delgado

et al., 2010; Guo et al., 2018; Kwon et al., 2016; Pathak et al., 2018). The present study uses a co-precipitation-based hydrothermal technique to synthesize Zn doped Ag_2O nanoparticles. For comparison, the current investigation uses the same protocol to prepare un-doped Ag_2O nanoparticles. X-ray diffraction (XRD) analysis and density functional theory (DFT) calculations were employed to investigate the position of the dopant atoms in the Ag_2O lattice. Appropriate DFT calculations were undertaken to find the change in the formation energy due to the doping of Zn in substitutional and interstitial sites of the Ag_2O supercell. The doped Ag_2O nanoparticle samples showed beneficial photocatalytic properties for degrading methyl orange (MO) and Rhodamine B (RhB) dyes in their aqueous solutions. Active species responsible for such photocatalytic features were revealed by conducting experiments in the presence of suitable scavenger molecules.

3.2 Experimental

3.2.1 Sample Preparation

The following hydrothermal co-precipitation protocol was followed to fabricate Zn doped silver oxide nanoparticles. The precursors were $Zn(NO_3)_2.6H_2O$ (SRLchem), $AgNO_3$ (Merck), and NaOH (Merck). All reagents were of analytical grade and used without further purification. All synthesis procedures used double distilled water. Three different molar ratios of $Zn(NO_3)_2.6H_2O$, and $AgNO_3$ (corresponding to 1.25, 2.5, and 5% Zn salt mole percent in overall composition) were dissolved in the proper volume of distilled water and mechanically stirred at 620 revolutions per minute. At the same time, 0.2M NaOH solution was added in a drop-wise manner until the pH of the mixture became nearly 11.24. Then the reaction mixture was transferred to a stainless steel autoclave in an oven at 150^{o}C. The heat treatment of the reaction vessel at this temperature continued for 24 hours. Symbols A1, A2, A3, and A4, denote the doped

samples corresponding to 1.25, 2.5, 5, and 10-mole percent Zn in the overall composition. The same protocol was employed to prepare pure Ag_2O (denoted by A0) nanoparticles. In this instance, $AgNO_3$ was the precursor. Note here, the initial step involved the dropwise addition of 0.2 M NaOH solution to a 2 mM $AgNO_3$ solution. With the addition of each drop of NaOH, a brown-colored precipitate was formed due to the following reaction.

$$AgNO_3 + NaOH \rightarrow AgOH \text{ (brown ppt)} \downarrow + NaNO_3$$

Precipitate formation continued till the addition of 12 ml NaOH solution. No further precipitate formation occurred after this because all Ag^+ had already been converted to AgOH. At this point, the pH of the solution mixture was ~11.

3.2.2 Computational Details

All theoretical calculations utilized the plane-wave density functional theory (DFT) in the Vienna ab-initio simulation package (VASP). The models investigated in the present research were made on the MedeA VASP software platform. The generalized gradient approximation Perdew-Burke-Ernzerhoff (PBE) exchange-correlation functional was used to calculate the defect formation energy as in reference (Perdew et al., 1996; Perdew & Wang, 1992). The Projected Augmented Wave (PAW) pseudopotential modeled the interaction between valence electrons and core-shell electrons. All calculations were performed using optimized parameters. The Kohn-Sham orbitals were expanded using the plane-wave basis set to a cut-off value of 800 eV with a $4 \times 4 \times 4$ k-point mesh size. The Ag_2O unit cell was multiplied to construct a $2 \times 2 \times 2$ supercell, followed by its geometry optimization and energy calculation. One model was built by substituting a Zn for an Ag at a lattice position in the original Ag_2O supercell (denoted by M1). In another model, the Zn occupies an interstitial site of the

Ag_2O supercell (represented by M2). One Zn atom was taken in the Ag_2O structure to mimic the dilute dopant concentration situation. The energies of the two models were separately calculated after optimizing their geometry. Figure 3.1(a), (b), and (c) display the optimized configurations of the Ag_2O supercell, M1 and M2, respectively. We also varied the supercell size of the Ag_2O unit cell. Energy per atom remains the same for all the calculations (in the Table 3.1), indicating that $2 \times 2 \times 2$ supercell size is enough for mimicking the nanoparticle.

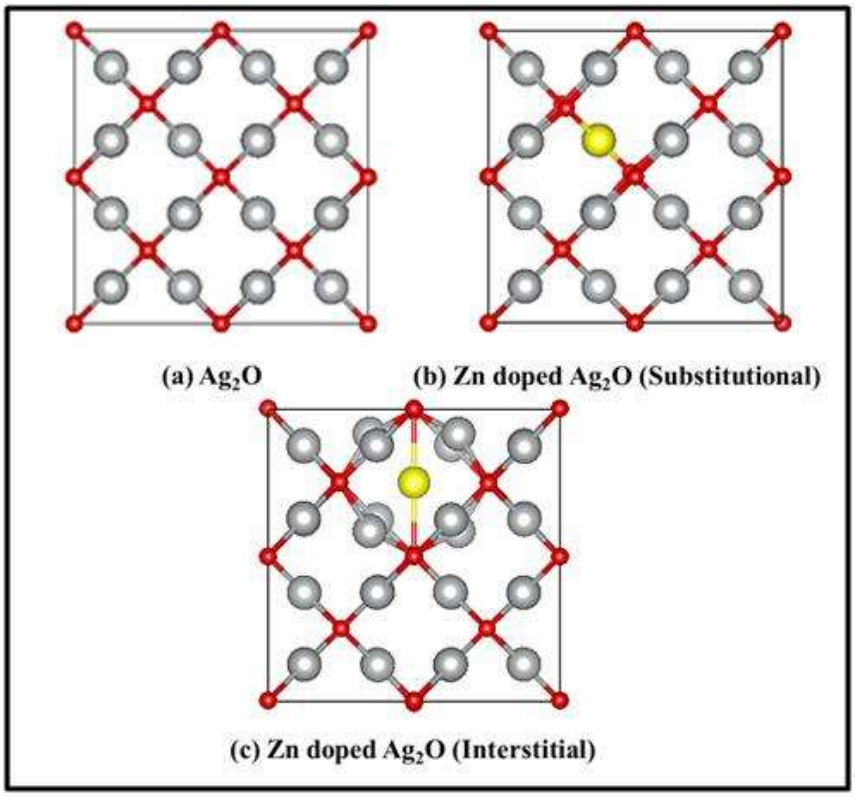

Figure 3.1 Optimized supercells of (a) Ag_2O, (b) Ag_2O with Zn substituting an Ag, and (c) Ag_2O with Zn placed in an interstitial position.

Table 3.1 Calculation of energy per atom with the variation supercell size of Ag_2O.

Supercell	No. of atoms	Energy per atom (E/atom) (eV)
$\mathbf{2 \times 2 \times 2}$	48	-3.57
$\mathbf{4 \times 2 \times 2}$	96	-3.57
$\mathbf{4 \times 4 \times 2}$	192	-3.57

Equation (3.1) gave the formation energy for the model with the substitutional defect (M1), while relation (3.2) was used to calculate the same for the interstitial defect system (M2).

$$E_f = E_{defect}(M1) - [E_{perfect}(Ag_2O) - \mu_{Ag} + \mu_{Zn}] \quad (3.1)$$

$$E_f = E_{defect}(M2) - [E_{perfect}(Ag_2O) + \mu_{Zn}] \quad (3.2)$$

Here E_f is the defect formation energy, $E_{defect}(M1)$ the energy of the M1, $E_{defect}(M2)$ the energy of the M2, μ_{Zn} and μ_{Ag} are the chemical potentials of Zn and Ag (Matsunaga et al., 2003; S. B. Zhang et al., 2001).

3.2.3 Photocatalytic Performance Measurements

The photocatalytic visible-light degradation of MO and RhB dyes was used to assess the activity of the doped Ag_2O samples. The reaction mixture of 2.4 ml aqueous solution of MO (concentration 4.7 mg/L) and 0.23 mg photocatalyst were mixed in a standard quartz cuvette of 1 cm path length. A few drops of 0.1 M HCl were added to reduce the pH of the reaction mixture to ~3.0. In the case of RhB degradation, 0.2 mg catalyst and 2.4 ml aqueous solution of RhB (concentration 4.7 mg/L) was used. Now the mixture (of photocatalyst and the aqueous solution of dye) was kept for five minutes under stirring in a dark environment. Only after this was the mixture subjected to visible light irradiation from 14W Philips cool white LED bulb to check the photocatalytic

activity of the photocatalyst. The absorption spectrum of the reaction mixture was measured after every two-minute interval. For the RhB degradation, the same was done after every three minutes interval. The efficiency of all the catalysts was compared through their turnover frequencies (TOF).

3.3 Results and Discussion

3.3.1 Structural Properties

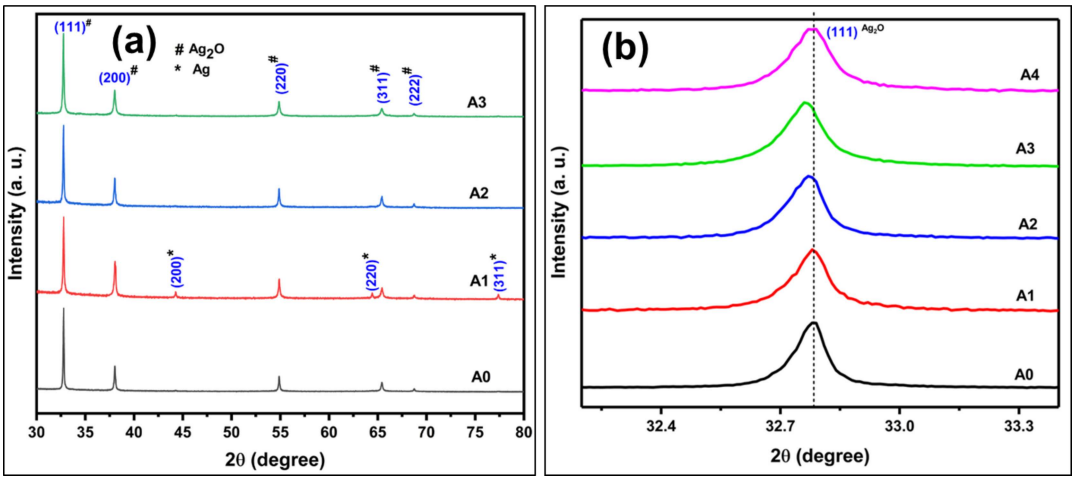

Figure 3.2 (a) Normalized HR-XRD patterns of pure Ag_2O (A0) and different Zn doped Ag_2O (A1, A2, A3) samples (b) Comparison of the Ag_2O (111) peaks with the increase in Zn doping (from the HR-XRD patterns).

Figure 3.2a shows high-resolution XRD spectra of undoped and Zn doped Ag_2O nanoparticle samples. All peaks in the XRD patterns of both doped and undoped Ag_2O nanoparticle samples match the standard diffraction patterns of the FCC Ag_2O (JCPDS Card No. 75-1532) phase. Note the Ag_2O structure on JCPDS card no. 75-1532 data is cuprite structured and has the cubic $P\bar{n}3m$ space group. These XRD patterns did not show any ZnO phase peaks. Figure 3.3 presents the XRD pattern of powder sample A4.

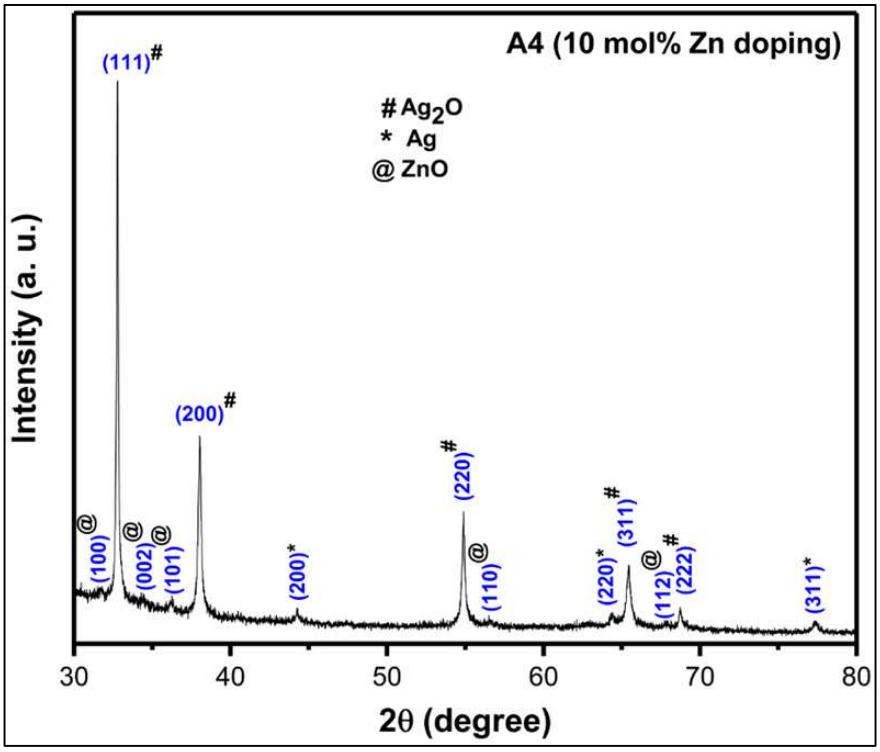

Figure 3.3 High-resolution XRD spectra of A4 (10 mol% Zn doping).

In contrast to other samples, it clearly shows the separate formation of the hexagonal ZnO phase (JCPDS Card No. 89-7102). Thus, on the addition of 10-mole percent Zn salt, the dopant could not be incorporated into the Ag_2O lattice, and a separate ZnO phase was also formed.

Figure 3.2b compares the positions of peaks corresponding to the (111) plane of various doped Ag_2O samples. The diffraction peak for the Ag_2O (111) plane shifts slightly to the left with an increase in Zn concentration from 1.25% to 5%. The shift towards a lower Bragg's angle increases with the percentage of the Zn dopant in the Ag_2O sample. Again, at 10% doping (A4), the (111) Ag2O peak does not shift, indicating that no doping occurred at this Zn salt addition level. Moreover, the sample A4 was also used for photocatalysis and exhibited the same efficiency as A0 (the pure Ag_2O nanoparticle sample). In view of this, detailed analysis and investigations were

only carried out on A1, A2, and A3. Figure 3.4 shows the SEM and corresponding EDS data of samples A1, A2, and A3. The data shows that the percentage of Zn increases with doping in A1, A2, and A3.

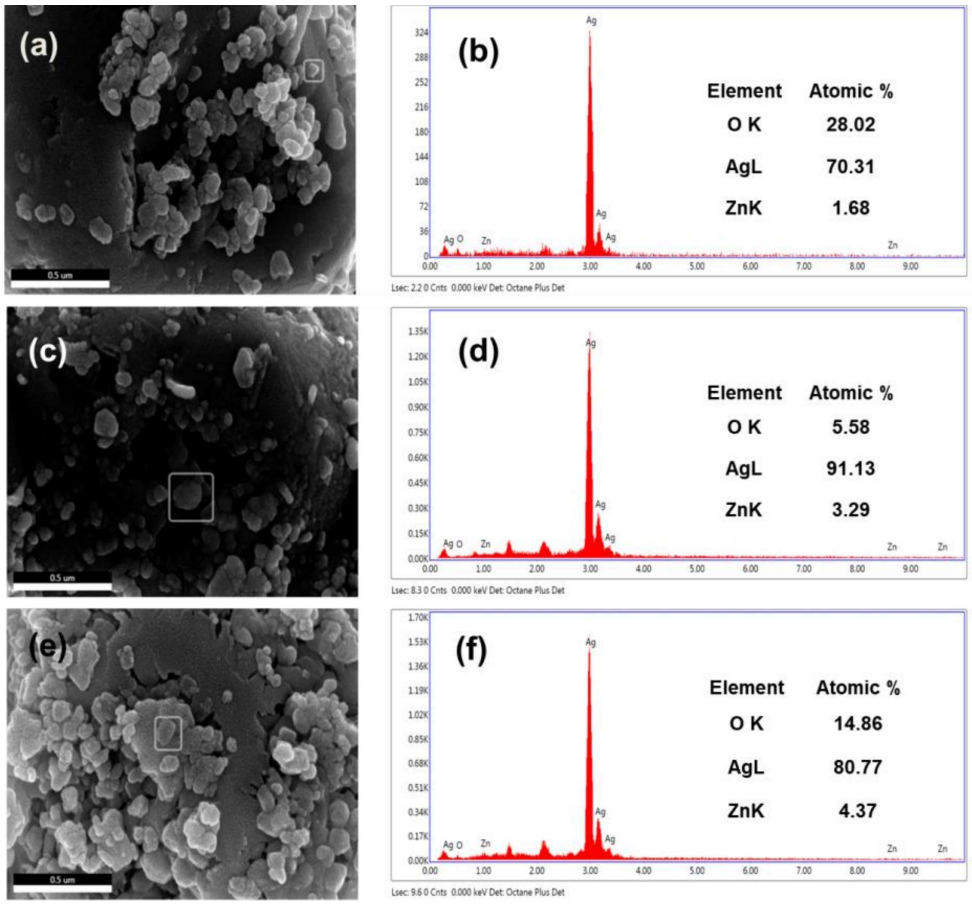

Figure 3.4 SEM images and corresponding EDS spectra of A1 (a, b), A2 (c, d), A3 (e, f) samples.

Thus, the change in Bragg angle corresponding to the (111) plane is maximum for 5% Zn doping with respect to the expansion of the Ag_2O lattice. When Zn goes into the Ag_2O lattice, it can enter an interstitial or a substitutional position. Substitution of the larger ion by a smaller one will result in the contraction of the lattice, while the incorporation of a larger ion into a smaller interstitial void expands the lattice (Q. Li et al., 2013; Wasastjerna, 1923). Accordingly, the expansion of the lattice tells us that the

dopant ions occupy vacant interstitial positions in the Ag_2O lattice. Table 3.2 presents the change in the lattice parameters calculated from the (111) plane XRD peak of doped and un-doped Ag_2O powder. Figure 3.5 displays the nature of change in the lattice parameter with doping. If we consider only the doped samples (A1 onwards), then a linear relation following Vegard's law may be invoked.

Table 3.2 Lattice parameter values found from XRD patterns.

Dopant concentrations (mol %)	Lattice parameter (Å)
0	4.7275
1.25	4.7278
2.5	4.7286
5	4.7305

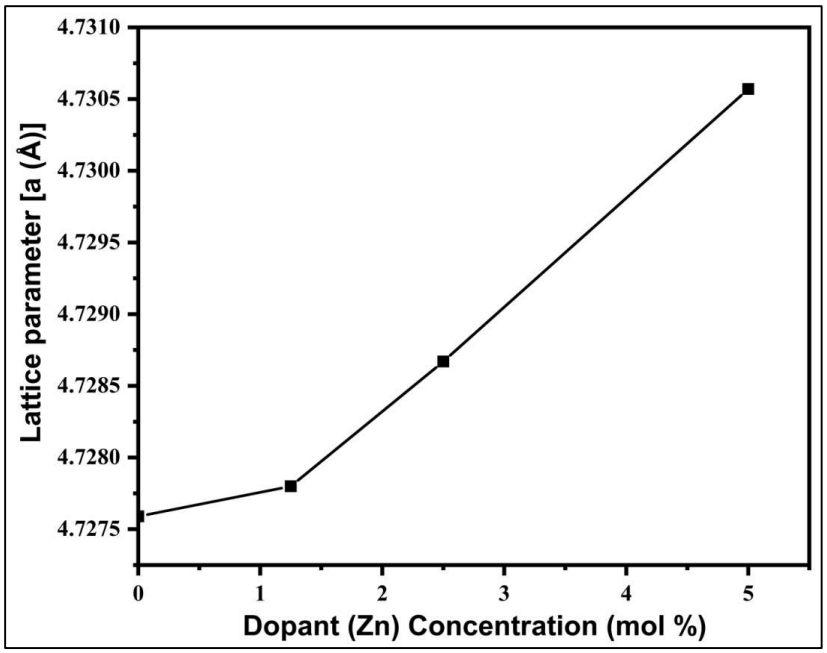

Figure 3.5 Variation in lattice parameter with Zn percentage.

3.3.2 DFT calculations

DFT calculations give additional evidence supporting the experimental findings. The defect formation energy for substitutional and interstitial defects are 0.52 eV and -0.96 eV, respectively, from the DFT calculations. Thus, interstitial doping is more favorable and agrees with the experimental results. Table 3.3 presents the expansion in dimensions due to the inclusion of a Zn in an interstitial position of the Ag_2O supercell. The calculated parameters show that the cubic Ag_2O lattice expands in all three directions, but the increase is lesser in the 'z' direction, which qualitatively conforms to the XRD results.

Table 3.3 The change in supercell dimensions with Zn in an interstitial position.

Dimension	Pure Ag_2O	After doping
X	9.620	9.678
Y	9.620	9.678
Z	9.620	9.647

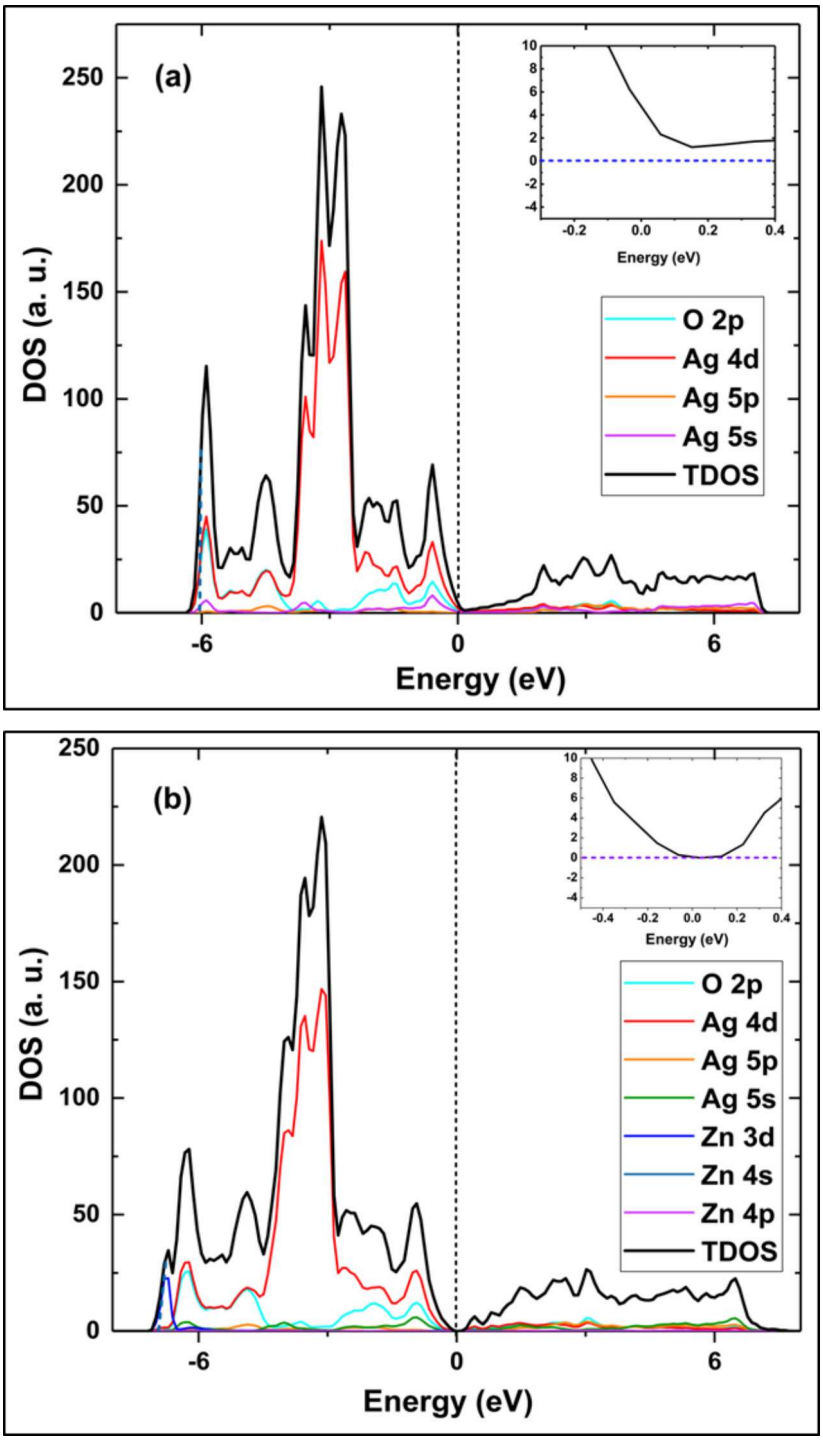

Figure 3.6 The density of states plots for (a) pure Ag_2O and (b) Zn doped Ag_2O.

It is well known DFT calculations underestimate bandgaps. The experimental band gap of pure Ag_2O is in the range of 1.2-1.5 eV. But, DFT calculations using GGA-

PBE functional give zero band gap (Yin et al., 2016). Such bandgap underestimation by the GGA-PBE DFT calculations is a well-known problem in the literature (Morales-García et al., 2017b). The bandgap underestimation can range from 100 (0 eV bandgap) to 50% of the experimental value. The GGA-PBE functional has a low computational cost but suffers from this bandgap underestimation problem. Limited computational resources at IIT(BHU) did not permit calculations by high-cost hybrid functional like HSE06 (hybrid functional), which can give comparatively accurate band gap (Nakanishi & Katayama-Yoshida, 2012; Shinde et al., 2020). Even then, the underestimated bandgap situation will also qualitatively carry the features of the density of states (DOS) and the band structure. Since the defect formation energy is more favorable for interstitial doping, therefore, the DOS and band structure calculations have been done on this optimized structure only. The present DFT calculations employ the GGA-PBE functional, which has earlier predicted a zero bandgap for pure Ag_2O (F. Pei et al., 2009). The DOS (Figure 3.6a) and the band structure (Figure 3.8a) results of our calculations also underestimate and predict a zero bandgap for Ag_2O. Figure 3.6b shows the DOS for the interstitially doped Zn-doped optimized structure. The inset in the figure clearly shows the presence of the finite bandgap (a small bandgap of ~0.2 eV) for the doped sample. The calculated band structure (Figure 3.8b) also shows a widening of the bandgap similar in magnitude to that found from the corresponding DOS (Figure 3.6b). A comparison of the doped and un-doped DOS shows that the valence band of the latter gets extended to ~7 eV (from ~6 eV in the pure Ag_2O). Furthermore, we see the emergence of Zn 3d dopant states at the lower edge of the valence band. Another critical observation is that, relative to the PDOS of Ag 4d and O 2p of the pure sample, the corresponding PDOS of Ag 4d and O 2p (of the doped sample) shifts to the left (Figure 3.7).

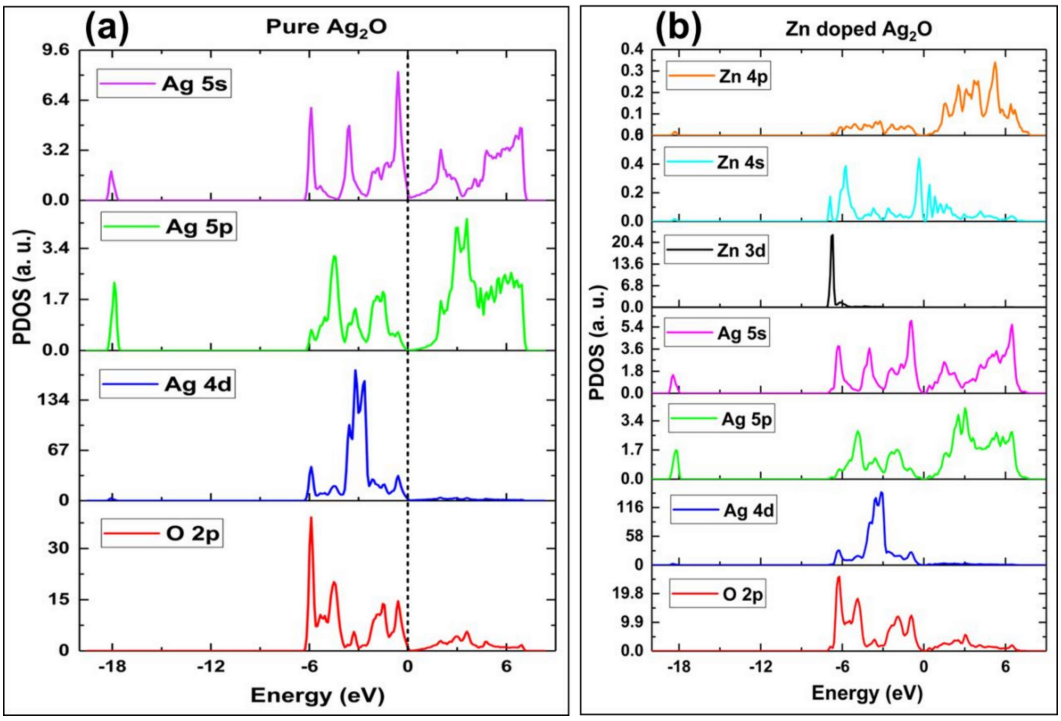

Figure 3.7 Partial density of states (PDOS) of (a) pure Ag_2O and (b) Zn doped Ag_2O.

Thus the first peak from the left of Ag 4d and O 2p is seen at values < -6 eV in the PDOS plot of the doped crystal structure. Contrary to this, the peaks in the PDOS of the pure crystal structure appear at values just greater than -6 eV. The shifting in these PDOS (of the doped crystal structure) seems to be due to the hybridization of the corresponding orbitals with that of Zn 3d orbitals (Endres et al., 2016; Pala et al., 2009). In effect, it lowers the valence band maximum (relative to the pure Ag_2O) and causes a widening of the bandgap.

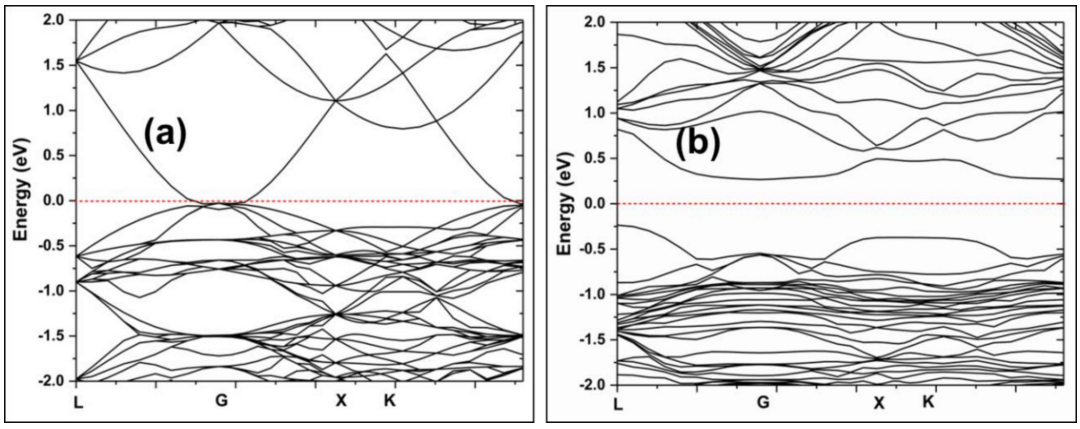

Figure 3.8 Band structures of (a) pure Ag_2O and (b) Zn doped Ag_2O.

3.3.3 TEM analysis

TEM images were used to analyze the morphology of the synthesized materials. The representative images show the formation of approximately spherical nanoparticles in all samples. TEM images of about 150 nanoparticles were sampled to calculate the particle size distributions. Sample A1 displays the smallest average particle sizes (~14.9 nm). The average particle size increases from 15.9 to 23.1 nm (Figure 3.10d and Figure 3.10f) with doping from 2.5 to 5% (samples A2 and A3). Thus, the particles in sample A1 (with 1.25% doping) are much smaller than those in A2 or A3. Sample A0 showed the greatest average particle sizes (~ 23.4 nm) (Figure 3.9). Note that, NaOH was added dropwise to the $AgNO_3$ solution. The AgOH nuclei formed earlier have more opportunity to grow while the nanoparticles from later nucleation are finer in size. This can give high value of polydispersity index (PDI). Apart from that, the nanoparticles were synthesized without surface stabilizer or capping agents. Hence, the agglomeration may also take place and increase the PDI.

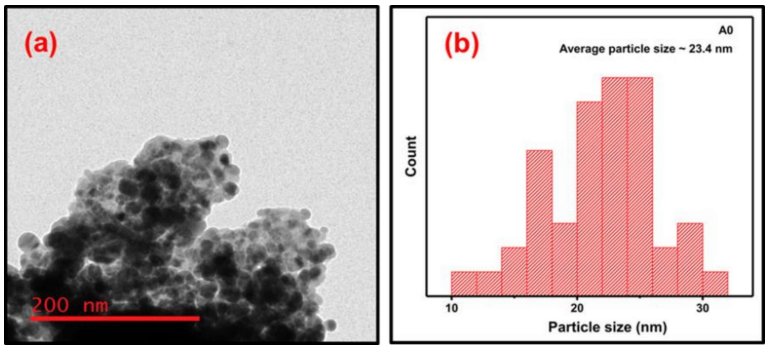

Figure 3.9 TEM analysis of A0.

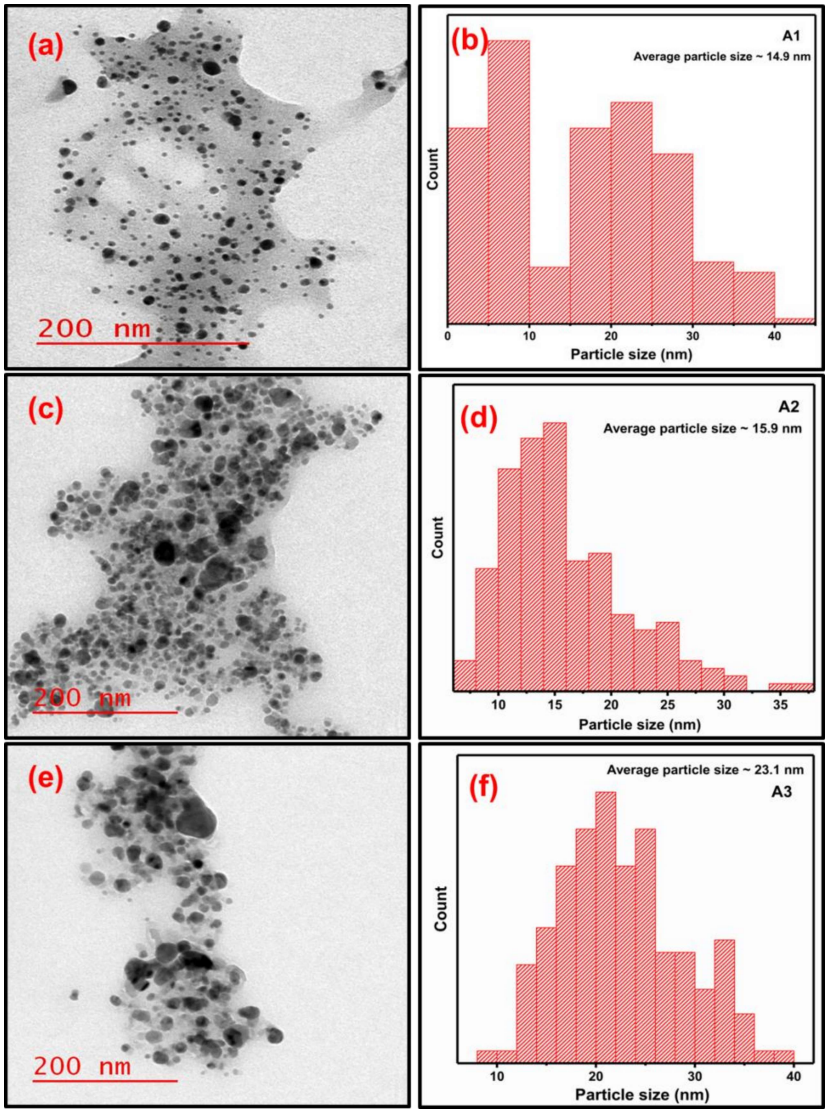

Figure 3.10 TEM images of Zn doped Ag_2O samples a) A1, c) A2, and e) A3. Part b), d), and f) present the particle size distributions corresponding to samples A1, A2, and A3, respectively.

3.3.4 XPS analysis

XPS characterization analyzed the binding states of different chemical species in samples A0 and A3. Figure 3.11 displays the high-resolution XPS spectra of Ag 3d and O1s of Ag_2O (A0) and Zn doped Ag_2O (A3). In both doped and pure samples, spin-orbit coupling splits the Ag 3d peak into Ag $3d_{5/2}$ and Ag $3d_{3/2}$ doublet. Figure 3.11a shows that the deconvolution of the Ag $3d_{5/2}$ region gives two peaks with binding energies (BE) 367.84 eV and 368.27 eV due to Ag_2O and Ag^0, respectively. The Ag $3d_{3/2}$ region of the same plot exhibits peaks corresponding to BE values 373.86 eV and 374.67 eV ascribed to Ag_2O and Ag^0, respectively.

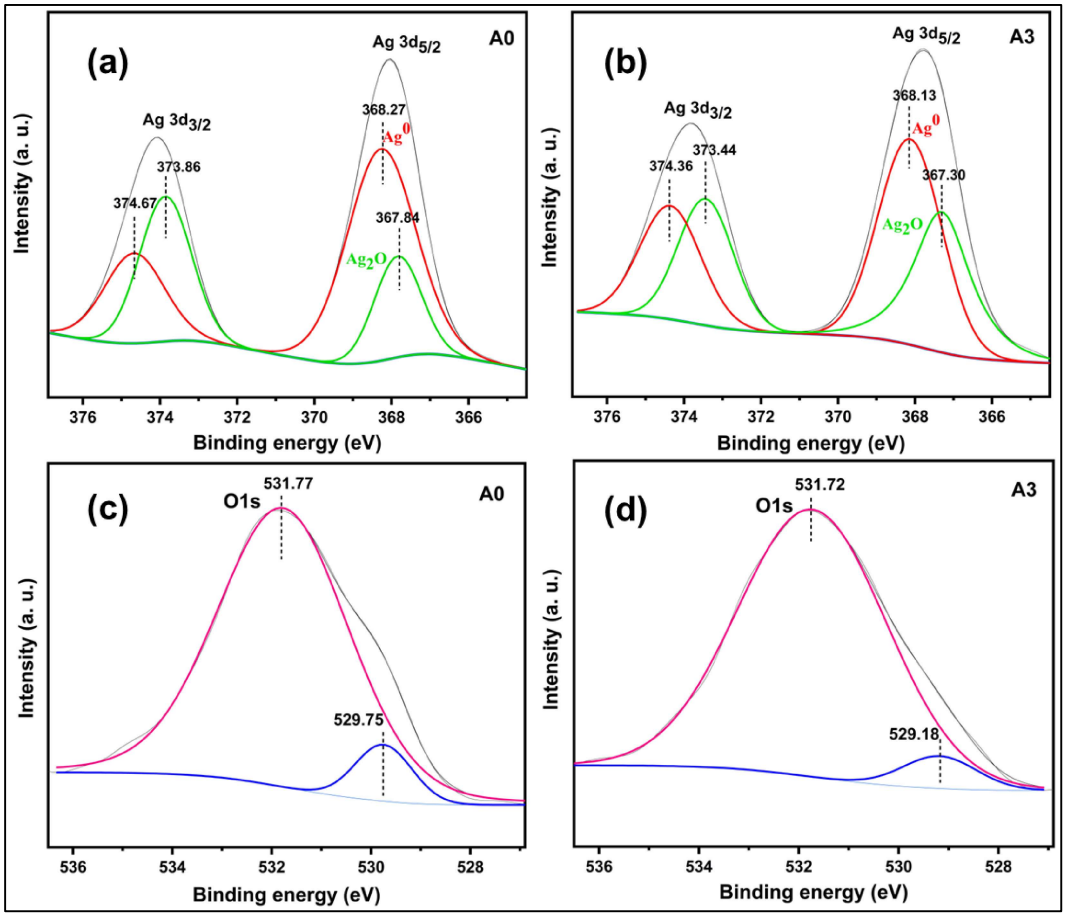

Figure 3.11 High resolution deconvoluted XPS spectra for (a,b) Ag 3d (samples A0 and A3) and (c,d) O1s (samples A0 and A3).

The deconvolution of Ag $3d_{5/2}$ peak of the XPS of sample A3 displayed peaks at 367.30, and 368.13 eV, while the Ag $3d_{3/2}$ gave peaks at 373.44 eV and 374.36 eV BE values. Compared with pure Ag_2O, the Ag 3d and O1s peaks of A3 shift toward lower BE values. It indicates an increase in electron density on the surface of the material due to the incorporation of the dopant in the semiconductor (Low et al., 2017). The shift towards lower BE values is characteristic of doping by an element of lower electronegativity than Ag.

3.3.5 Bandgap analysis

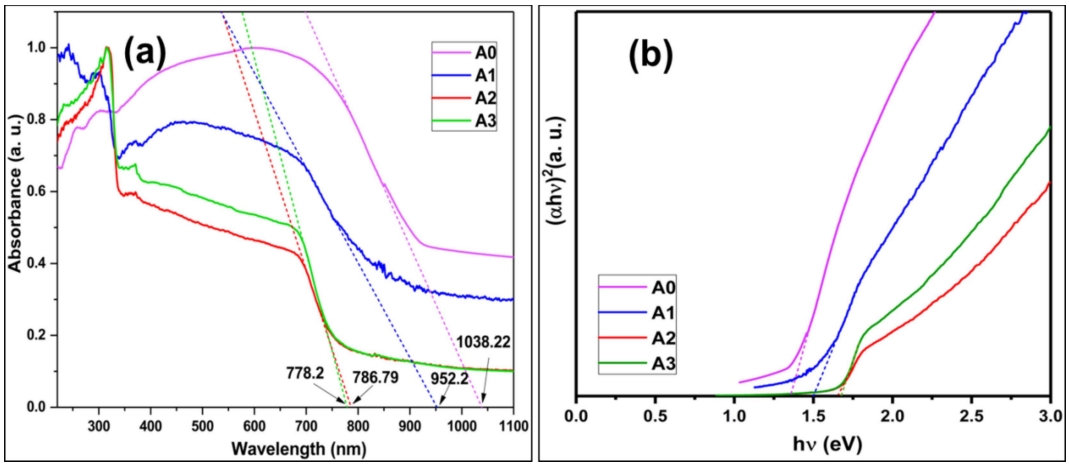

Figure 3.12 (a) UV-Visible absorption spectra and (b) Tauc plots of prepared samples A0, A1, A2, and A3.

Bandgap values are required to elucidate the mechanism of photocatalysis. The solid-state absorption spectra of the all the prepared samples are provided in Figure 3.12a. The Tauc plot is derived from the absorption data and shown in Figure 3.12b. Table 3.4 gives the band gaps calculated from the Tauc plot and directly from the absorbance plots. The tauc plots were constructed using the following relation:

$$(\alpha h\vartheta)^{1/n} = (h\vartheta - E_g) \qquad (3.3)$$

The intercept of the tangent to the linear part of the plot on the x-axis gives the bandgap energies of these doped materials. Samples A0, A1, A2, and A3 exhibit bandgap energies of 1.35, 1.50, 1.64, and 1.65 eV, respectively. The bandgap increases with Zn doping and is significant compared to the generally observed value of 1.2 (to 1.5) eV for pure Ag_2O nanoparticles (Xuefei Wang et al., 2011; C. Yu et al., 2014). However, the increase in bandgap from A2 to A3 is quite small.

Table 3.4 Comparison of band gap of the synthesized samples by different methods.

Samples	Band gap from absorption spectra (eV)	Band gap from tauc plot (eV)
A0	1.19	1.35
A1	1.30	1.50
A2	1.58	1.64
A3	1.59	1.65

3.3.6 Fluorescence spectra

Figure 3.13 displays the fluorescence spectra of the A0, A2, and A3 samples. The excitation wavelength was 400 nm for all samples. The Brownian motion of the dispersed nanoparticles cause the noisy spectra of the samples (Loumaigne et al., 2015). The fluorescence intensities of doped materials (A1, A2, A3) were lower than pure Ag_2O (A0). Moreover, the fluorescence intensity of A3 was the least. Photoluminescence (PL) emission is directly associated with the recombination of photo-excited holes and electrons. Hence, lower PL intensity demonstrates a delay in recombination and, thus, better photocatalytic activity (Gupta et al., 2020; V. Kumar et al., 2017; Q. Wang et al., 2014). It seems that doping Ag_2O with Zn^{2+} ions causes the formation of surface trapping sites due to the difference in metal ion charges. Such trap sites selectively capture photo-excited electrons or holes and reduce photoluminescence intensity by preventing recombination. Higher doping percentages induce more such trap sites that prevent recombination.

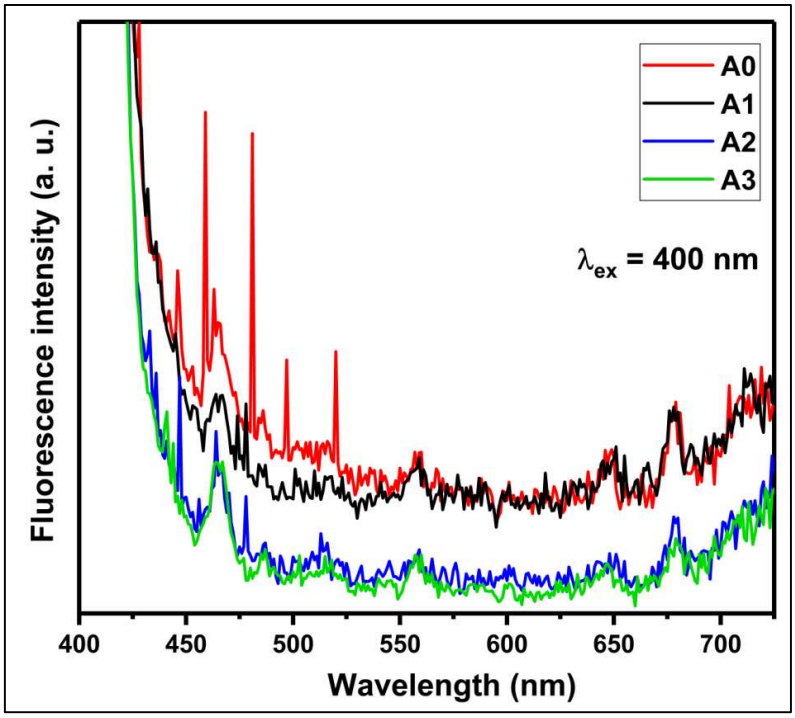

Figure 3.13 Photoluminescence spectra of samples A0, A1, A2, and A3.

3.3.7 Photocatalytic activity

The photocatalytic activity and reusability of the prepared samples were evaluated for the degradation of methyl orange (MO) and Rhodamine-B (RhB) under visible light irradiation.

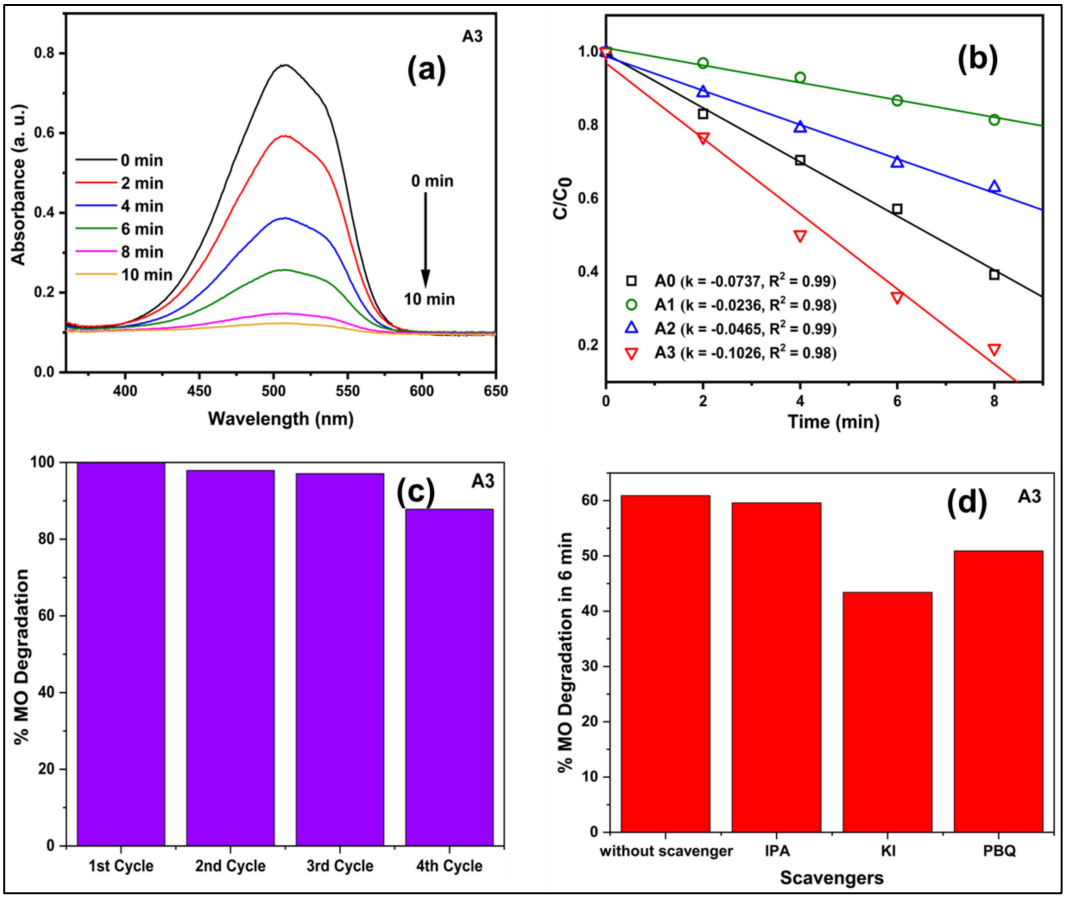

Figure 3.14 (a) Photocatalytic MO degradation of A3 (b) Comparison of photocatalytic performance of the different photocatalysts (c) Recyclability of A3 (d) Result of active species trapping experiments for A3 catalyst in the presence of various scavenger molecules.

Figure 3.14a displays the UV-visible absorbance spectra for aerobic MO degradation (in its aqueous solution), and Figure 3.15 shows the UV-visible absorption spectra for aerobic RhB degradation in the presence of A3 photocatalyst.

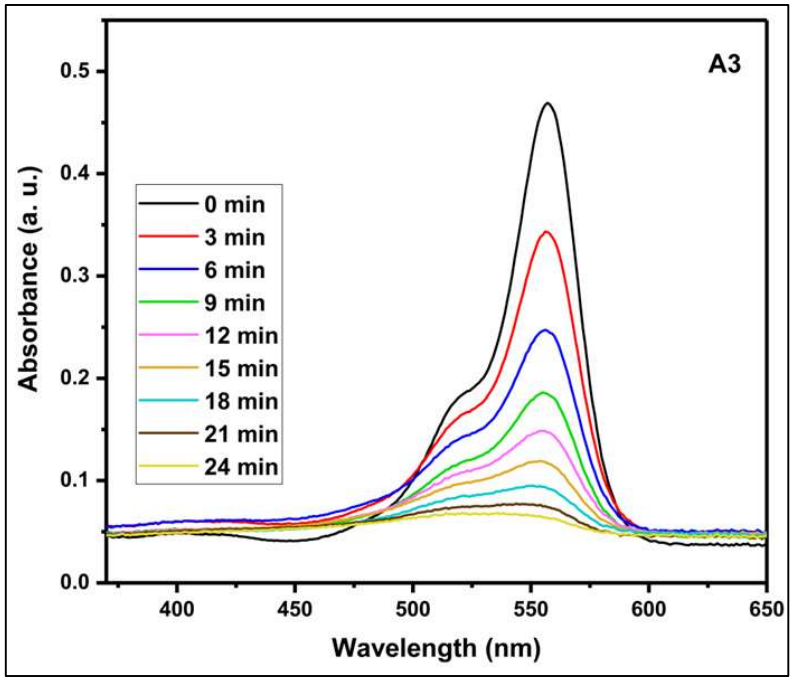

Figure 3.15 Change in the UV-visible spectrum of RhB (showing its degradation) on visible light irradiation with time in the presence of the A3 photocatalyst sample.

In the absence of catalysts, there is no degradation of dyes. Figure 3.16 indicates no degradation of MO in the absence of catalysts.

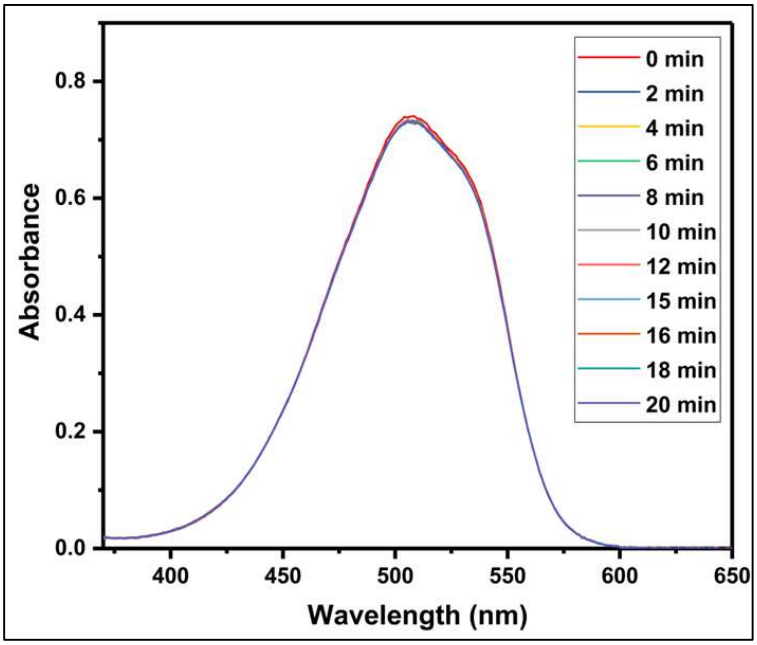

Figure 3.16 UV-visible of an aqueous solution of MO under cool white LED visible light irradiation (without photocatalyst). In the absence of a photocatalyst, there is no change in the intensity of the MO UV-visible absorbance under the light.

The photocatalyst degrades MO almost entirely in a short period of ten minutes. Please note that experiments were also done at different pHs to find the optimum condition for photocatalytic MO degradation. Figure 3.17 displays the change in photocatalytic activity of the sample A3 with pH (for MO degradation). Sample A3 shows the best photocatalytic activity at pH ~3. Thus HCl was added to bring the reaction medium pH to the desired level. Lower pH favors better interaction between the catalyst and pollutants (Yi et al., 2018).

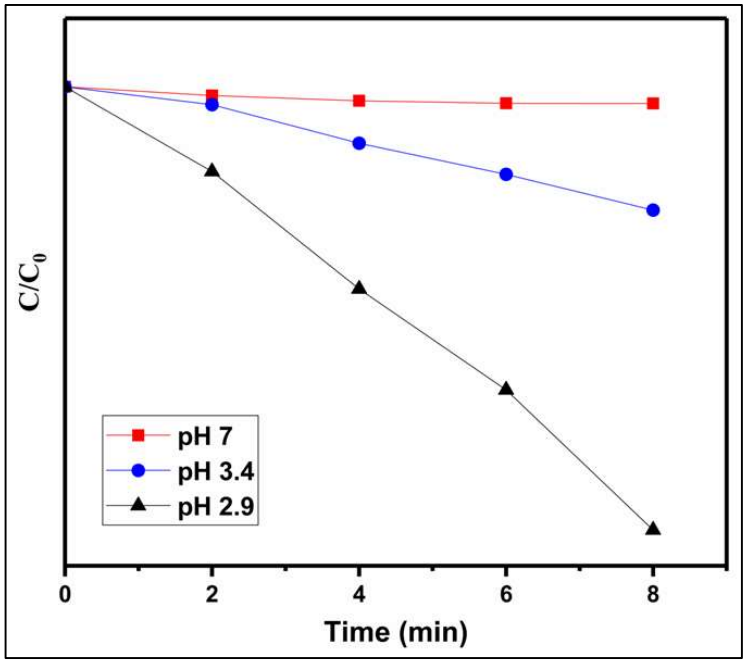

Figure 3.17 Degradation of MO at different pH in the presence of A3 photocatalyst.

Figure 3.14b compares the photocatalytic performance of pure Ag_2O and different doped Ag_2O photocatalysts. All considered samples degrade MO by zero-order kinetics. The rate constant increases with doping, and photocatalyst A3 exhibits the best degradation kinetics. Surprisingly, MO degradation in the presence of pure Ag_2O is faster than on samples A1 and A2. Hence, the initial effect of doping is that it decreases their photocatalytic efficiency compared to pure Ag_2O. But on increasing the doping percentage to 5%, the photocatalytic activity becomes better than pure Ag_2O. The trend is similar for the visible light degradation of RhB (Figure 3.18). The kinetics of RhB degradation is nearly the same in the presence of A0 and A2, while it is quickest for A3.

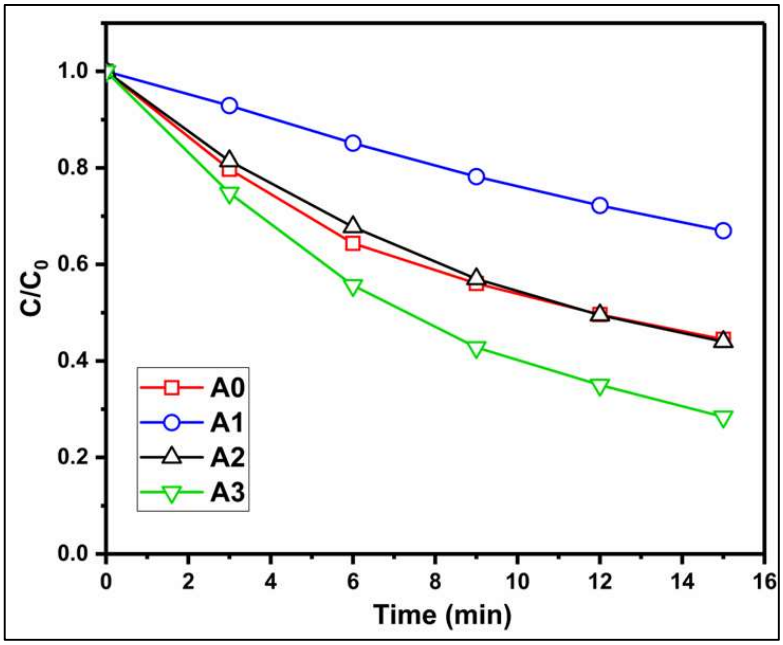

Figure 3.18 RhB degradation kinetic plots for sample catalysts (A0, A1, A2, and A3).

Table 3.5 and Table 3.6 give details of the corresponding turnover frequency values and rate constants for MO degradation and RhB degradation, respectively.

Table 3.5 A comparison of turnover frequencies (TOF) of MO on the prepared doped Ag_2O photocatalysts.

Photocatalyst	**Light source**	**The apparent rate constant (min^{-1})**	**TOF (moles $g^{-1}min^{-1}$)**
A0 (0 % dopant)	Cool white LED (14W)	0.0763	2.54×10^{-5}
A1 (1.25 % dopant)	Same	0.0254	8.01×10^{-6}
A2 (2.5 % dopant)	Same	0.0488	1.60×10^{-5}
A3 (5 % dopant)	Same	0.1099	2.72×10^{-5}

Table 3.6 A comparison of turnover frequencies (TOF) of the visible light aerobic degradation of RhB on the prepared doped Ag_2O photocatalysts.

Photocatalyst	Light source	The apparent rate constant (min^{-1})	TOF (moles $g^{-1}min^{-1}$)
A0 (0 % dopant)	Cool white LED (14W)	0.0491	1.85×10^{-5}
A1 (1.25 % dopant)	Same	0.0244	5.68×10^{-6}
A2 (2.5 % dopant)	Same	0.0475	1.21×10^{-5}
A3 (5 % dopant)	Same	0.0635	1.99×10^{-5}

Active species trapping experiments were carried out using photocatalyst A3 to understand the mechanism of photocatalytic reactions. Reactive species like $OH^{\cdot}$, $O_2^{\cdot -}$ and h^+ play an essential role in the aerobic photocatalytic degradation of several organic pollutants. The molecule p-benzoquinone (PBQ) was used to scavenge $O_2^{\cdot -}$ radical, potassium iodide (KI) was the hole scavenger, and isopropyl alcohol (IPA) consumed the $OH^{\cdot}$ radicals generated during aerobic MO degradation reaction. Figure 3.14d represents the results of the trapping experiments for A3. The experimental results showed that the presence of KI inhibited the degradation of MO more than other scavengers. It indicates that holes are the most generated reactive species during the reaction. The superoxide scavenger, PBQ, also affects photocatalytic activity. Its effect is second only to KI. The order of activity of the reactive species for the catalyst is $h^+ > O_2^{\cdot -} > OH^{\cdot}$.

Visible light irradiation photo-excites the doped Ag_2O, causing the generation of holes at the VB and electrons at the CB. The main driving force for photocatalytic degradation of MO is the production of holes (the reactive species). Thus, MO gets oxidized at the VB, transferring its electrons to the photo-generated holes. Concurrently,

the photo-excited electron reduces the oxygen in the water to superoxide radicals, which then transform into hydroxyl radicals (through well-known routes) to oxidize MO molecules.

While the fluorescence spectrum intensity decreases with doping, the photocatalytic activities for aerobic degradation of MO and RhB do not follow the same order. As mentioned earlier, this implies that the surface trap sites increase with Zn^{2+} doping resulting in better charge separation and, consequently, less intense fluorescence spectrums. DFT calculation results indicate the other reason for this observation. Zn doping extends and shifts the position of the Ag_2O valence band by introducing dopant energy states in it. The generated photoexcited holes get transferred to the dopant energy states. Figure 3.19 gives a schematic illustrating the proposed mechanism of photocatalysis. Nevertheless, the photocatalytic activity of undoped Ag_2O (A0) is nearly the same as A2. Only A3 displays better photocatalytic activity than A0.

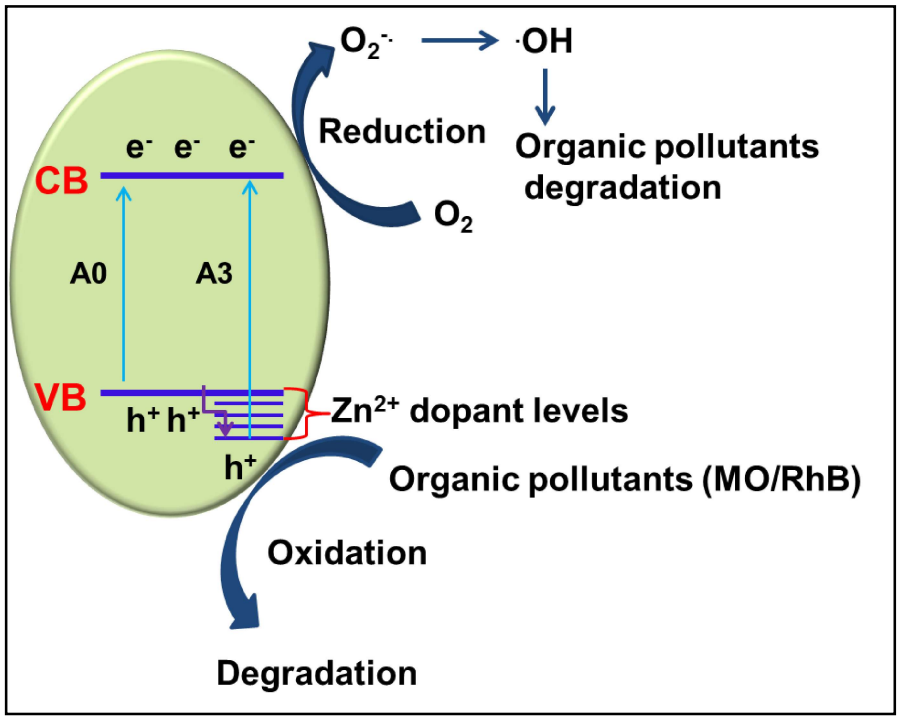

Figure 3.19 Schematic diagram of the proposed mechanism during photocatalysis.

Photocatalytic activity is determined not only by charge separation but also by the adsorption of the substrate on the catalyst surface. The present photocatalytic reaction follows a photo-excited hole dominated substrate (MO or RhB) oxidation mechanism. A vital step of such a mechanism is the adsorption of the substrate on the surface of the catalyst (J. Yan et al., 2013). It seems that doping with Zn (up to 1.25-mole percent) weakens the surface adsorption behavior of the catalyst towards these molecules. On further increase in doping, the adsorption behavior becomes better than that of A0, and hence A3 displays the best photocatalytic activity towards these dye molecules.

3.4 Conclusions

Zn-doped Ag_2O nanoparticles were prepared by a hydrothermal method. XRD pattern analysis shows that the unit cell parameters of Ag_2O expand with Zn doping. DFT calculations show Ag_2O lattice expansion on interstitial Zn doping. The calculated formation energy of interstitially Zn-doped Ag_2O was lesser than the model with Zn substituting an Ag establishing the higher stability of the former. The optical bandgap of 5-mole percent Zn-doped Ag_2O widens to 1.65 eV. The DFT calculated density of states and band structure of the interstitially doped model gave an insight into the change in electronic structure that led to the bandgap widening phenomenon. The dopant Zn 3d states increased the size of the valence band and also lowered the position of its maximum. Photoluminescence spectroscopy points to increased charge separation with doping. The doped photocatalysts demonstrate photocatalytic MO and RhB degradation. But, the photocatalytic activity exceeds that of undoped Ag_2O only after reaching the 5-mole percent doping level. The best-doped photocatalyst also demonstrates excellent recyclability in photocatalytic efficiency. Reactive species trapping experiments with

individual scavenger molecules showed that the photocatalysis proceeds by a photo-excited hole dominated mechanism. It appears that doping not only widens the bandgap but also affects the substrate adsorption behavior of the catalyst.